Biomaterials 101 (2016) 121–130

Contents lists available at ScienceDirect

Biomaterials

journal homepage: www.elsevier.com/locate/biomaterials

Redoxable heteronanocrystals functioning magnetic relaxation switch for activatable T_1 and T_2 dual-mode magnetic resonance imaging

Myeong-Hoon Kim [a], Hye-Young Son [b], Ga-Yun Kim [a], Kwangyeol Park [b], Yong-Min Huh [b, c, **], Seungjoo Haam [a, *]

[a] Department of Chemical and Biomolecular Engineering, College of Engineering, Yonsei University, Seoul, 120-749, Republic of Korea
[b] Department of Radiology, College of Medicine, Yonsei University, Seoul, 120-752, Republic of Korea
[c] YUHS-KRIBB Medical Convergence Research Institute, Yonsei University College of Medicine, Seoul, 120-752, South Korea

ARTICLE INFO

Article history:
Received 3 March 2016
Received in revised form
30 May 2016
Accepted 30 May 2016
Available online 1 June 2016

Keywords:
Magnetic nanoparticles
Dual-mode contrast agent
MR imaging
Glutathione
Stimuli-responsive

ABSTRACT

T_1/T_2 dual-mode magnetic resonance (MR) contrast agents (DMCAs) have gained much attention because of their ability to improve accuracy by providing two pieces of complementary information with one instrument. However, most of these agents are "always ON" systems that emit MR contrast regardless of their interaction with target cells or biomarkers, which may result in poor target-to-background ratios. Herein, we introduce a rationally designed magnetic relaxation switch (MGRS) for an activatable T_1/T_2 dual MR imaging system. Redox-responsive heteronanocrystals, consisting of a superparamagnetic Fe_3O_4 core and a paramagnetic Mn_3O_4 shell, are synthesized through seed-mediated growth and subsequently surface-modified with polysorbate 80. The Mn_3O_4 shell acts as both a protector of Fe_3O_4 in aqueous environments to attenuate T_2 relaxation and as a redoxable switch that can be activated in intracellular reducing environments by glutathione. This simultaneously generates large amounts of magnetically decoupled Mn^{2+} ions and allows Fe_3O_4 to interact with the water protons. This smart nanoplatform shows an appropriate hydrodynamic size for the EPR effect (10–100 nm) and demonstrates biocompatibility. Efficient transitions of OFF/ON dual contrast effects are observed by *in vitro* imaging and MR relaxivity measurements. The ability to use these materials as DMCAs is demonstrated *via* effective passive tumor targeting for T_1- and T_2-weighted MR imaging in tumor-bearing mice.

1. Introduction

Magnetic resonance (MR) imaging has been widely applied in a variety of clinical diagnostic fields as a powerful noninvasive technique [1,2]. MR imaging is particularly appealing because it can provide anatomical images of tissues and organs with excellent spatial resolution [3,4]. The diagnostic capabilities of MR imaging can be greatly improved by introducing exogenous medical media, such as T_1 or T_2 contrast agents, for enhanced target tissue contrast on T_1-or T_2-weighted imaging sequences, respectively [5,6]. T_1 contrast agents, represented by clinically-available gadolinium (Gd^{3+}) chelates, are paramagnetic materials, which shorten the longitudinal relaxation time (T_1) of nearby water protons [7,8]. However, despite their ability to generate a positive (bright) contrast with high signal intensity, the use of T_1 contrast agents is compromised by their lack of sensitivity and intrinsic low MR relaxivity [9]. Alternatively, T_2 contrast agents commonly consist of superparamagnetic nanoparticles, such as superparamagnetic iron oxide nanoparticles (SPION), and can be magnetically saturated by the typical magnetic field strengths in MRI scanners [2,10]. These agents work by shortening the traverse relaxation time (T_2) of water protons in their vicinity [11,12]. While they have high detection sensitivity for lesions, their magnetic susceptibility to artifacts and inherent negative (dark) contrast effects can induce low signal-to-noise ratios, which limits their application [13,14]. Consequentially, MR contrast agents that integrate both T_1 and T_2 contrast capabilities are highly desirable for advanced MR imaging techniques [14,15]. These dual-mode agents are able to overcome the limitations of individual T_1 and T_2 imaging modalities by improving the accuracy. This is done by validating the reconstruction and visualizing the data that is simultaneously provided by

* Corresponding author.
** Corresponding author. Department of Radiology, College of Medicine, Yonsei University, Seoul, 120-752, Republic of Korea.
E-mail addresses: ymhuh@yuhs.ac (Y.-M. Huh), haam@yonsei.ac.kr (S. Haam).

http://dx.doi.org/10.1016/j.biomaterials.2016.05.054
0142-9612/

two complementary sources of information within a single instrument [15,16].

Recent investigations into T_1/T_2 dual-mode contrast agents (DMCAs) have evolved to combine T_1 and T_2 contrast agents into a single nanoprobe [13,16–19]. In this case, severe proton relaxation interference between the two different contrast agents (magnetic coupling), which attenuates the T_1 contrast effect by the strong local magnetic field of the superparamagnetic T_2 material, is inevitable when they are in close proximity to one another [15,16]. Several designs have demonstrated that inserting distance modulators between the T_1 and T_2 materials, such as silica shells [13,15] or inorganic linkers [16], can reduce the undesirable magnetic coupling effect. For those nanoplatforms, however, fastidious processing of the nanoparticles and well-defined DMCA design are required to avoid quenching the T_1 and T_2 contrast effects. Furthermore, most of the contrast agents are "always ON" systems, exerting the MR contrast effect regardless of their proximity or interaction with target cells or environmental markers in biology; this can result in poor target-to-background ratios [20,21].

The development of inventive imaging strategies based on stimuli-responsive smart nanosystems with high T_1 and T_2 relaxivity would be an ultimate solution and enable accurate imaging of biological targets. In particular, the redox potential variation induced by concentration changes of reducing agents across different intra/extracellular regions has been one of the most extensively employed biological triggers for stimuli-responsive imaging nanoparticles [22,23]. Glutathione (GSH) is an abundant reducing agent in cytoplasm (1~15 mM), which plays a central role in cell growth and function [24,25]; the fact that cancer cells have higher GSH concentrations than corresponding normal cells enables redox-responsive nanoplatforms to be promising cancer diagnostic probes [24,26]. Therefore, the introduction of a redox-responsive moiety that can cage T_1 and T_2 contrast agents in a magnetically coupled state and initially shield them from water molecules would greatly improve the MR signal transition in stimuli-responsive DMCA systems for cancer diagnosis.

In this study, we developed an activatable T_1/T_2 dual-mode imaging probe with a magnetic relaxation switch (MGRS) that exhibits high sensitivity and effective silencing/activation of the MR contrast effect in target conditions. This was accomplished by constructing heteronanocrystals that consist of a superparamagnetic core and a redox-responsive paramagnetic shell. For a proof of concept, we designed a Mn_3O_4-coated Fe_3O_4 hybrid nanocrystal that is encapsulated within amphiphilic polyethylene glycol (PEG) derivatives; we refer to these crystals as redox-responsive activatable nanostarshells (RANS). They can be activated under an intracellular reducing environment for ultrasensitive bimodal MR imaging *in vivo*. To date, various Mn-based materials, such as Mn chelates [27], MnO nanoparticles [28], and hybrid nanomaterials [11,29], have been applied for MR imaging with good biocompatibility. However, the application of a redoxable Mn_3O_4 layer as the MGRS of a DMCA has not been reported. The schematic illustration in Fig. 1 depicts the design of RANS and its operation mechanism. The Fe_3O_4 core of RANS is initially shielded from the aqueous environment by the Mn_3O_4 shell. The Mn center is also restricted within the Mn_3O_4 structure, resulting in low accessibility to water and magnetic coupling with the superparamagnetic core [30]; the T_1 and T_2 contrast effects are quenched ("OFF" state). After accumulation of RANS on the tumor tissue, which is caused by the enhanced permeation and retention (EPR) effect, and subsequent internalization into the tumor cells, the Mn_3O_4 shells are dissolved into Mn^{2+} ions by a redox reaction ("redox-mediated peeling") in the presence of abundant GSH in the cytoplasm. Numerous high-spin Mn^{2+} ions and exposed Fe_3O_4 cores can individually serve as MR contrast agents; these can be collectively activated to generate a dramatic enhancement in the T_1 and T_2 signal contrast ("ON" state). The heteronanocrystals were synthesized by sequential seed-mediated growth using an iron precursor and a manganese precursor through a thermal decomposition method. Using an emulsion and solvent evaporation method, these nanocrystals were subsequently transferred into an aqueous solution using polysorbate 80 (P80) as a biocompatible capping molecule. The transition efficacy of the OFF/ON dual contrast effects and the potential usefulness of RANS as a DMCA were confirmed through *in vitro* and *in vivo* experiments.

2. Materials and methods

2.1. Materials

Iron (III) acetylacetonate, manganese (II) acetylacetonate, 1,2-hexadecanediol, oleic acid (OA, 90%, technical grade), oleylamine (70%, technical grade), polysorbate 80 (P80), benzyl ether, *N*-ethylmaleimide (NEM), and α-lipoic acid (LA) were purchased from Sigma Aldrich. Reduced glutathione (GSH) was obtained from Tokyo Chemical Industry. Phosphate-buffered saline (PBS; 0.010 M, pH 7.4), Roswell Park Memorial Institute medium (RPMI), and fetal bovine serum (FBS) were purchased from Gibco. Centrifugal filters (MW cut-off: 50 kDa) were obtained from Millipore. All chemicals and reagents were of analytical grade and used as-received without further purification.

2.2. Synthesis of superparamagnetic iron oxide (Fe_3O_4) nanoparticles

Monodispersed Fe_3O_4 nanoparticles were prepared using the reported thermal decomposition method [9]. In a typical reaction, iron (III) acetylacetonate (2 mmol), 1,2-hexadecanediol (10 mmol), oleic acid (6 mmol), and oleylamine (6 mmol) were dissolved in benzyl ether (20 mL) and magnetically stirred under an ambient nitrogen atmosphere. The mixture was pre-heated to 200 °C for 2 h and then refluxed at 300 °C for 1 h. After being cooled down to room temperature (RT), the product was purified with excess ethyl alcohol three times and dispersed in hexane.

2.3. Synthesis of redox-responsive activatable nanostarshells (RANS) and P80-coated Fe_3O_4 nanoparticles (P80-IO)

Mn_3O_4-coated Fe_3O_4 (IO@MO) heteronanocrystals were prepared by a seed-mediated growth method using Fe_3O_4 nanoparticles as seeds. 20 mg of Fe_3O_4 nanoparticles in hexane were injected into an oleylamine (18.7 mL) solution containing 110 mg of manganese (II) acetylacetonate. The solution was vacuumed at 100 °C for 1 h and heated to 180 °C under an ambient nitrogen atmosphere. The reaction mixture was maintained at this temperature for 6 h and then cooled to RT to form a brownish suspension. The product was precipitated after centrifugation at 3000 rpm for 10 min and then re-dispersed into 2 mL of hexane. Ethyl alcohol (20 mL) was added to the solution and precipitated after centrifugation at 10,000 rpm for 10 min. The resulting nanocrystals were re-dispersed in hexane. Hydrophilic RANS was prepared by encapsulation of the hydrophobic surface of the IO@MO nanoparticles with a PEG shell; this was done using a nano-emulsion method in order to make the nanocrystals biocompatible and dispersible in aqueous media for use in biomedical applications. IO@MO nanoparticles (10 mg) were dissolved in 2 mL of hexane, which was then mixed with 20 mL of a P80 aqueous solution (5 mg/mL). After mutual saturation of the organic and aqueous phases, the emulsion was ultra-sonicated in a bath for 20 min at 450 W. The resulting suspension was stirred overnight at RT to evaporate the

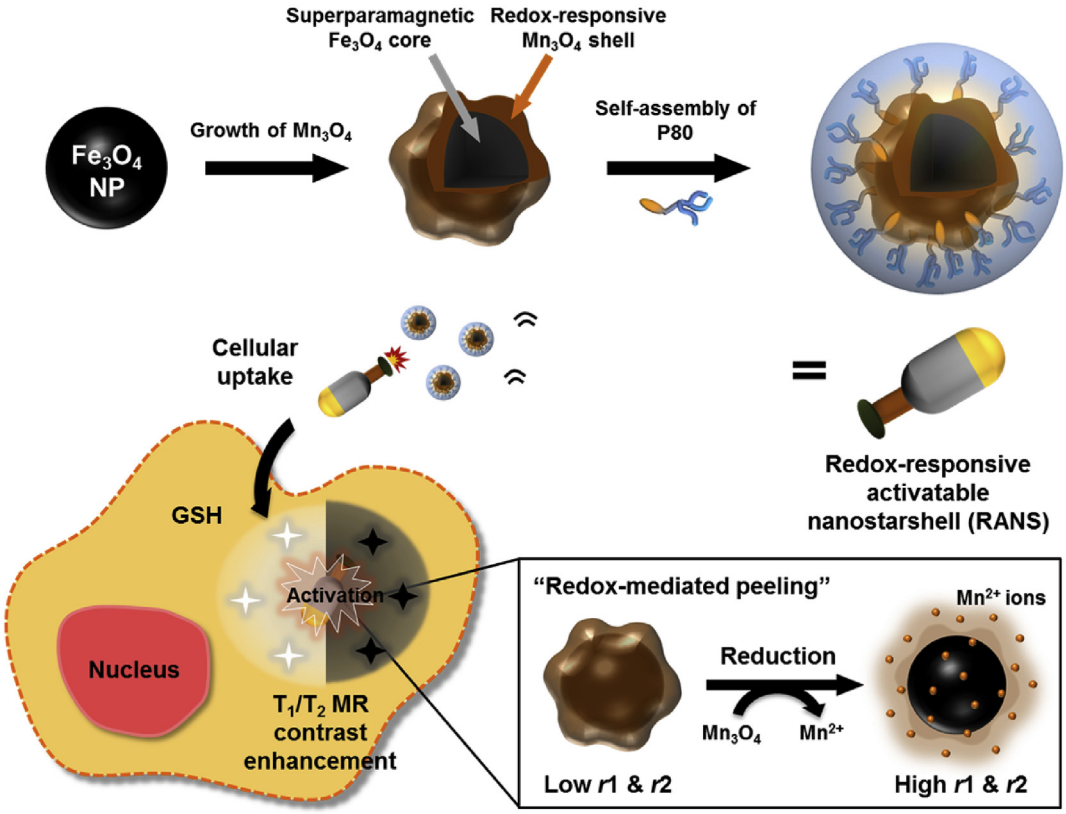

Fig. 1. Schematic illustration of the redox-responsive activatable nanostarshell (RANS). Superparamagnetic Fe_3O_4 nanoparticle (NP) was coated with redox-responsive Mn_3O_4 shell by seed-mediated growth through thermal decomposition method, and surface-modified with polysorbate 80 (P80). This nanoplatform performs like a starshell containing flares (Fe_3O_4 cores and paramagnetic Mn-holding Mn_3O_4 shells) to illuminate the target area (enhancement of MR signal contrast of diagnostic interests) through "redox-mediated peeling" by intracellular glutathione (GSH).

organic solvent and purified by three cycles of centrifugal filtering for 20 min each at 3200 rpm. The products were re-dispersed in deionized water. P80-IO was synthesized by encapsulation of the Fe_3O_4 nanoparticles with P80 using the same procedures used for the synthesis of RANS.

2.4. Characterization

The morphology of the Fe_3O_4 nanoparticles, IO@MO nanoparticles, and RANS was evaluated using a transmission electron microscope (TEM; JEM-2100, JEOL Ltd.) that was equipped with an energy-dispersive X-ray spectrometer (EDS). The magnetic hysteresis loop and the saturation magnetization of the Fe_3O_4 nanoparticles and IO@MO nanoparticles were measured in dried samples at 298 K using a vibrating sample magnetometer (VSM; Model-7300, Lakeshore). The crystalline structure of the Fe_3O_4 nanoparticles and IO@MO nanoparticles was determined by analyzing X-ray diffraction (XRD) patterns that were obtained on a Rigaku Miniflex X-ray diffractometer (Rigaku Corporation, Japan) at 298 K. The hydrodynamic diameters of RANS and P80-IO were measured *via* laser scattering (ELS-Z, Otsuka Electronics). X-ray photoelectron spectroscopy (XPS) experiments were performed with a K-alpha system (Thermo U.K.). The absorbance of RANS and P80-IO was analyzed using a UV–vis spectrometer (Optizen 2120UV, MECASYS).

2.5. In vitro cytotoxicity test using the MTT assay

The cytotoxicity of Mn^{2+} ($MnCl_2$) and RANS on MKN-45 cells (human gastric cancer cell line, American Type Culture Collection (ATCC), USA) was evaluated with a colorimetric assay based on the mitochondrial oxidation of 3-(4,5-dimethylthiazol-2-yl)-2,5-diphenyltetrazolium bromide (MTT) using a cell proliferation kit (Roche). MKN-45 cells (1×10^4 cells per well) were plated in 96-well plates, incubated in RPMI (containing 10% FBS and 1% antibiotics-antimytotic) at 37 °C in a humidified atmosphere with 5% CO_2, and treated with various concentrations (0–14 μg_{metal} mL^{-1}) of either Mn^{2+} or RANS for 24 h. The relative percentage of cell viability was then determined as the ratio between the formazan intensity in the viable cells treated with the materials and the intensity in non-treated cells; this is shown as an average ± standard deviation ($n = 4$). Non-treated cells were normalized to 100% cell viability.

2.6. Cellular uptake of RANS

MKN-45 cells (2.0×10^7 cells) were implanted in a Petri dish at 37 °C overnight and washed three times using PBS (pH 7.4). These were then treated with various concentrations (1, 2, and 5 μg_{metal} mL^{-1}) of RANS solutions for 4 h. Subsequently, the cells were washed with PBS three times to eliminate any free RANS, detached using trypsin, collected, and then re-suspended in 200 mL of a 4% paraformaldehyde solution. The cellular internalization was verified by TEM (JEOL-1100) and MR imaging.

To reduce or increase the concentration of GSH before treating the RANS solutions, the MKN-45 cells were pretreated with NEM (a GSH scavenger: 0.01 mM and 0.05 mM) or LA (a GSH synthesis enhancer: 0.05 mM and 0.1 mM) for 10 min and washed with PBS.

2.7. Animal experimental procedure

A xenograft tumor model was used to investigate tumor imaging with RANS. MKN-45 cells (2.0×10^7 cells) suspended in 50 μL of saline per mouse were injected into the proximal thigh of male BALB/c-nude mice (4–5 weeks of age, $n = 3$). All animal experiments were conducted with the approval of the Institutional Animal Care and Use Committee, Yonsei University Health System.

2.8. In vitro and in vivo MR imaging

In vitro MR imaging experiments were performed using a 1.5 T clinical MRI instrument with a micro-47 surface coil (Intera; Philips Medical Systems, Best, The Netherlands). The a) T_1 or b) T_2 weights of the RANS solutions and RANS-treated cells were measured with the Carr-Pur-cell-Meiboom-Grill sequence at RT with the following parameters: a) point resolution of 0.234 mm × 0.234 mm, section thickness of 3 mm, TE = 18 ms, TR = 625 ms, and number of acquisitions = 2 and b) point resolution of 0.156 mm × 0.156 mm, section thickness of 0.6 mm, 32 echoes with 12 ms even echo space, TR = 10 s, and number of acquisitions = 1. For acquisition of a) T_1-or b) T_2-weighted MR images of the RANS-treated cells, the following parameters were adopted: a) point resolution of 0.234 mm × 0.234 mm, section thickness of 3 mm, TE = 18 ms, TR = 625 ms, and number of acquisitions = 2 and b) point resolution of 0.234 mm × 0.234 mm, section thickness of 0.6 mm, TE = 60 ms, TR = 4000 ms, and number of acquisitions = 1.

In vivo MR imaging experiments were performed using a 3 T clinical MRI instrument with a wrist coil (Intera; Philips Medical Systems, Best, The Netherlands). For a) T_1- and b) T_2-weighted MR imaging in the nude mouse model, we adopted the following parameters: a) point resolution of 0.234 mm × 0.234 mm, section thickness of 1.0 mm, TE = 12.7 ms, TR = 694 ms, and number of acquisitions = 1 and b) point resolution of 0.234 mm × 0.234 mm, section thickness of 1.0 mm, TE = 70 ms, TR = 2635 ms, and number of acquisitions = 1.

3. Results and discussion

The strategy to synthesize redox-responsive activatable nanostarshells (RANS) involves sequential crystallization of Fe_3O_4 nanoparticles and epitaxial growth of Mn_3O_4 shells on the nanoparticle surface *via* seed-mediated growth based on a thermal decomposition method. To obtain efficient magnetic coupling between T_2 and T_1 materials, Fe_3O_4 and Mn_3O_4 were designed to be directly contacted as a core/shell heteronanocrystal structure. The superparamagnetic Fe_3O_4 nanoparticles, located in the core of RANS, were synthesized as previously reported and dispersed in hexane [9]. The Fe_3O_4 nanoparticles were transferred to an oleylamine solution of manganese (II) acetylacetonate and reacted at 180 °C for further growth of the Mn_3O_4 shell. The monodispersed Fe_3O_4 nanoparticles (10.2 ± 1.2 nm, $n > 30$) and Mn_3O_4-coated Fe_3O_4 (IO@MO) nanoparticles (13.3 ± 2.0 nm, $n > 30$) were observed in transmission electron microscopy (TEM) images (Fig. 2a and b). The spherical Fe_3O_4 nanoparticles adopted a popcorn-like shape after growth of the Mn_3O_4 shell because Mn_3O_4 nucleation occurred simultaneously at several sites on the surface of Fe_3O_4. The energy dispersive X-ray spectroscopic (EDS) analysis shows that the products are composed of Fe, Mn, and O elements (Fig. S1). The Cu and C peaks are attributed to the copper grid and carbon support film. To quantify the molar ratio of the core/shell metal composition, we measured the amount of Fe and Mn in IO@MO nanoparticles by inductively coupled plasma optical emission spectrometry (ICP-OES). The molar ratio between Fe and Mn in the sample was approximately 1:1.2, which corresponds to the molar ratio between Fe_3O_4 and Mn_3O_4 in IO@MO, as calculated from their size and density (Fe_3O_4: 5.18 g/cm^3 and Mn_3O_4: 4.86 g/cm^3) [31] using the formula $n = 4\rho\pi r^3/3$ MW (n = mole, ρ = density, r = radius, and MW = molecular weight). This demonstrates that the change in shape is entirely attributed to the growth of the Mn_3O_4 shell. The magnetic properties of the Fe_3O_4 and IO@MO nanoparticles, confirmed from the magnetic hysteresis loop taken at 298 K with a vibrating sample magnetometer (VSM), indicated the superparamagnetic behavior of the nanoparticles, which is in accordance with major property of Fe_3O_4 nanoparticles (Fig. 2c and d). The metal contents of the VSM samples were obtained by ICP-OES. Fe_3O_4 nanoparticles showed a high saturated magnetization value (105.6 emu/mass of Fe) at 1.5 T. The IO@MO nanoparticles exhibited a similar magnetization value (106.0 emu/mass of Fe), suggesting that the magnetic properties of the IO@MO nanoparticles were mainly derived from the core Fe_3O_4 nanoparticles; this is the case because the Mn_3O_4 shell exhibited paramagnetic properties with a weak magnetization increase. The X-ray diffraction (XRD) patterns in Fig. S2 show that the crystallinity of Fe_3O_4 is preserved (JCPDS Card No. 88–0315) and that a Mn_3O_4 phase, with small characteristic peaks, is formed (JCPDS Card No. 24–0734).

To imbue the nanoparticles, which have been stabilized by a hydrophobic capping agent, with water-solubility, the as-synthesized IO@MO nanoparticles were surface-modified with polysorbate 80 (P80), possessing tri-armed polyethylene glycol (PEG) chains, through a nano-emulsion method. This process is based on the fact that the oleyl groups of both the capping agents and P80 have high hydrophobic interactions. The resulting RANS displayed good colloidal stability in aqueous solutions without aggregation, even after they were left for several months at RT. Dynamic light scattering (DLS) analysis was performed to measure the hydrodynamic size and aqueous dispersibility of the resultant RANS. P80-coated Fe_3O_4 nanoparticles (P80-IO) were prepared for comparison. As shown in Fig. S3, both P80-IO and RANS exhibited narrow size distributions in water with single scattering peaks located at 20.8 ± 5.1 nm and 21.9 ± 4.6 nm, respectively. This size is appropriate for passive tumor targeting due to the enhanced permeability and retention (EPR) effect [32,33].

Before evaluating the performance of RANS as a DMCA, we first confirmed the redox-responsive ability of RANS by measuring its physicochemical changes in the presence of glutathione (GSH). GSH is an abundant tripeptide in cytoplasm; its presence creates a reducing environment [24,26,34]. The morphological change of RANS after reduction by a GSH solution (10 mM) was observed by analyzing TEM images (Fig. 3a). The Mn_3O_4 shell of RANS was dissolved into Mn^{2+} ions by reduction. Additionally, the popcorn-shaped RANS (left image) adopted a spherical shape, leaving Fe_3O_4 cores (right image) with the initial size of Fe_3O_4 nanoparticles (before Mn_3O_4 growth). The size of RANS in the 10 mM GSH solution was 20.6 ± 4.6 nm with narrow size distribution (Fig. S3c). The surface atomic composition of RANS was determined by X-ray photoelectron spectroscopy (XPS) (Fig. 3b). Since the inorganic shell of RANS was comprised of Mn_3O_4, Mn provided two peaks (Mn $2p_{1/2}$ and Mn $2p_{3/2}$), which were attributed to Mn_3O_4 (652.6 and 641.2 eV, respectively). After the Mn_3O_4 surface was peeled by the GSH solution, the Fe peaks (Fe $2p_{1/2}$ at 724.3 eV and Fe $2p_{3/2}$ at 710.6 eV) increased and the Mn peaks decreased. This occurred because the core Fe_3O_4 and a little part of Mn-doped Fe_3O_4 were exposed to the outer surface after the shell was dissolved and washed away. The response of RANS to GSH was determined by examining the UV–vis absorbance spectra. RANS and P80-IO both exhibited similar absorbance spectra, declining from under 400 nm to higher wavelengths in deionized water (DW); this behavior is attributed to the absorbance of Fe_3O_4 and Mn_3O_4 (Fig. 4a and b).

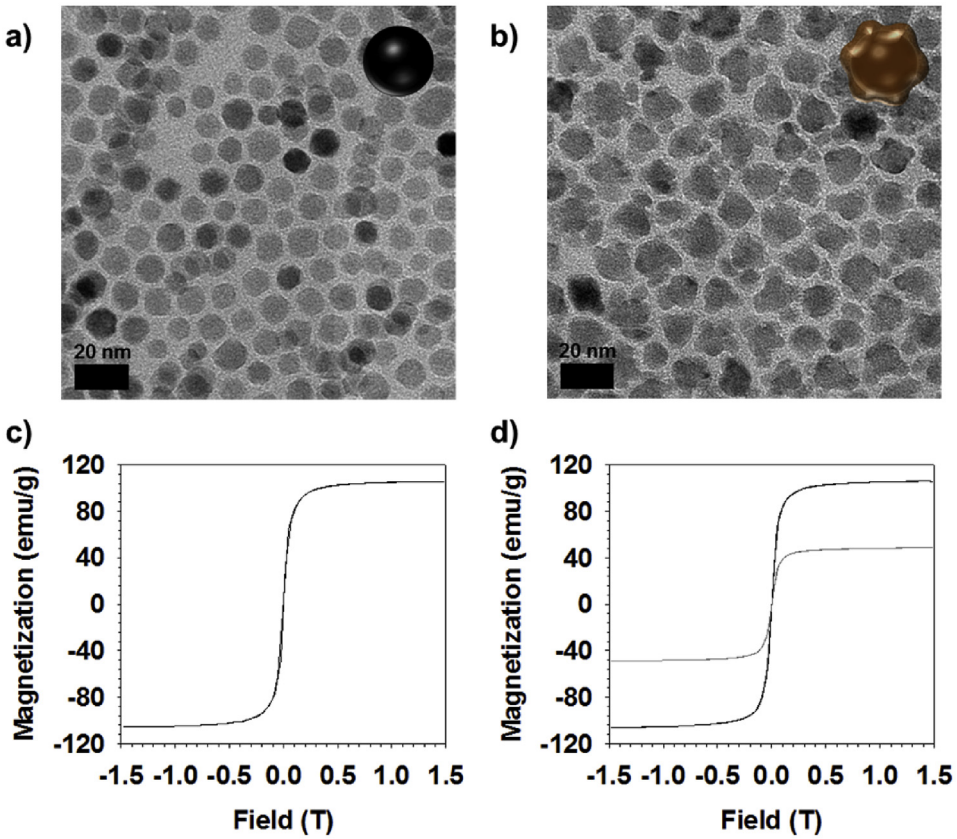

Fig. 2. TEM images of a) Fe_3O_4 nanoparticles (10.2 ± 1.2 nm) and b) IO@MO nanoparticles (13.3 ± 2.0 nm). Magnetic hysteresis loop of c) Fe_3O_4 nanoparticles and d) IO@MO nanoparticles (black line: emu/mass of Fe, gray line: emu/mass of Fe + Mn).

When dispersed in a 10 mM GSH solution, the absorbance of RANS decreased immediately due to dissolution of the Mn_3O_4 shell into Mn^{2+} ions. Alternatively, the absorbance of P80-IO remained unchanged because the Fe_3O_4 nanoparticles were durable in the reducing environment that was induced by GSH. The peeling of Mn_3O_4 in the RANS solution was completed within 30 min under millimolar (0.5–5 mM) GSH concentrations (Fig. S4a and b). To verify that RANS is durable in acidic conditions and only responsive in a reducing environment, we analyzed the pH-dependent changes of absorbance of RANS without GSH (Fig. S4c). In the absence of GSH, no immediate changes in the absorbance features of RANS were seen at an acidic pH (pH 5.5) over a period of 100 min. As shown in Fig. 4c, RANS and P80-IO were well-dispersed in the DW, pH 5.5 PBS buffer solution, and 10 mM GSH solution; they did not experience any aggregation. The brown colour of the RANS solution turned to a lighter brown after redox-mediated peeling of the Mn_3O_4 shell by GSH. These observations further support the idea that RANS is specifically responsive to reducing environments.

The redox-dependent structural and physicochemical transformation of RANS in water was expected to affect the proton relaxation change in a magnetic field (Fig. 5a). The superparamagnetic Fe_3O_4 core, which generates a strong local magnetic field, is a major contributor to T_2 relaxivity [12]. The Mn_3O_4 shell exhibits intrinsic magnetic properties as a T_1 contrast agent [30]. In the initial conditions, before the MGRS activation of RANS in a reducing environment, the paramagnetic Mn centers are confined within the Mn_3O_4 crystal structure so that their exposure to water is limited compared to that of free Mn^{2+} ions. We also hypothesized that the strong magnetic field induced by the large magnetic moment of the superparamagnetic Fe_3O_4 core would perturb the relaxation process of the significantly weaker paramagnetic Mn_3O_4 shell (magnetic coupling), resulting in quenching of the T_1 signal. To evaluate the effectiveness of RANS as an activatable T_1/T_2 contrast agent, we incubated RANS with DW and a GSH solution (10 mM) for 2 h and obtained T_1- and T_2-weighted MR images (Fig. 5b and c). The RANS solutions of different concentrations in DW exhibited low r_1 and r_2 relaxivities of 2.4 mM^{-1} s^{-1} and 92.2 mM^{-1} s^{-1}, respectively (black lines in Fig. 5d and e). Interestingly, the r_2 relaxivity of RANS was lower than that of the control (P80-IO) as a T_2 contrast agent (197.3 mM^{-1} s^{-1}, Fig. S5). This demonstrated the strong silencing effect between the Fe_3O_4 core and Mn_3O_4 shell, inhibiting both the local magnetic field and the water interactions of the Fe_3O_4 core. After MGRS activation in the GSH solution, the T_1-weighted MR image of RANS exhibited much stronger positive contrast enhancement than that of RANS in the GSH-free DW; a 6.8-fold increase of r_1 relaxivity was observed (16.1 mM^{-1} s^{-1}). In addition, an obvious darkening contrast effect in the T_2-weighted MR image was observed, and the r_2 relaxivity increased by a factor of 2.8 (258.6 mM^{-1} s^{-1}). Alternatively, the r_1 and r_2 relaxivities of P80-IO nanoparticles were unchanged in the presence of GSH (Fig. S5). To account for the greatly enhanced MR relaxivities, the following facts must be considered. (1) The water coordination number to Mn centers increased due to the release of numerous high-spin Mn^{2+} ions upon the dissolution of Mn_3O_4 shells; therefore, large amounts of Mn^{2+} ions, which individually serve as T_1 contrast agents, were collectively activated to generate strong enhancements in T_1-weighted MR imaging. (2) Water molecules could easily penetrate and come into contact with Fe_3O_4 cores, and the magnetic field barriers of the superparamagnetic Fe_3O_4 cores were removed by elimination of the concrete Mn_3O_4 shells. (3) The

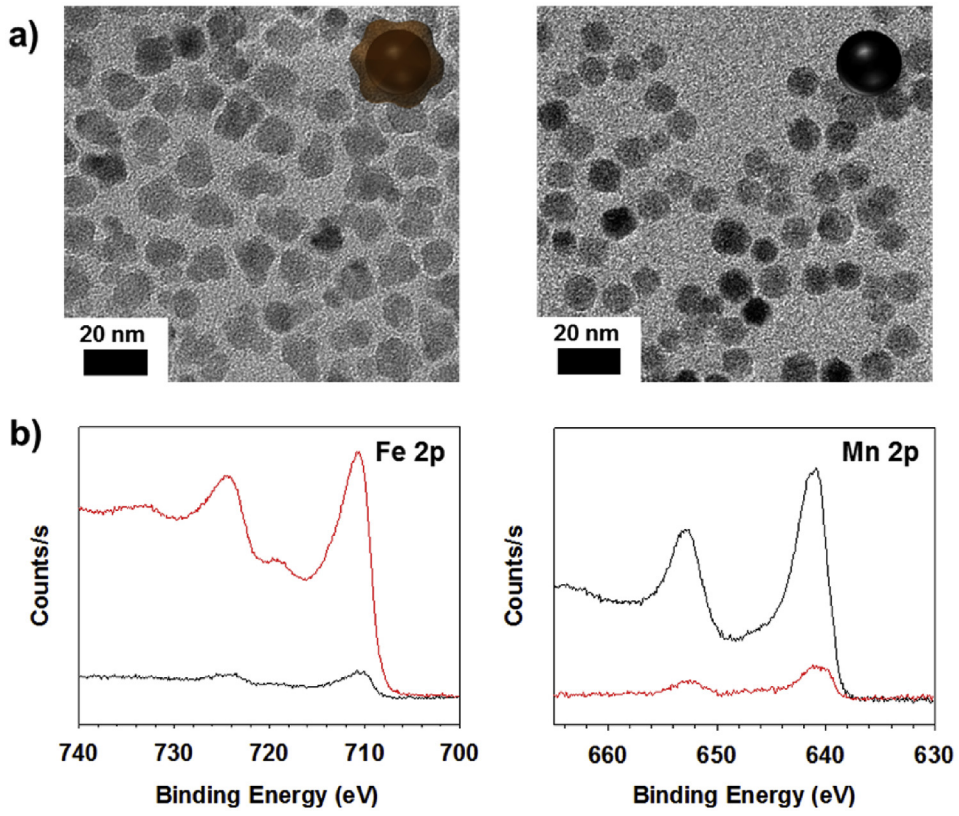

Fig. 3. a) TEM images of RANS in DW (left) and RANS after dispersed in 10 mM GSH solution for overnight (right). b) XPS spectrum of Fe 2p (left) and Mn 2p (right) level (black line: RANS, red line: RANS separated after dispersion in 10 mM GSH). (For interpretation of the references to colour in this figure legend, the reader is referred to the web version of this article.)

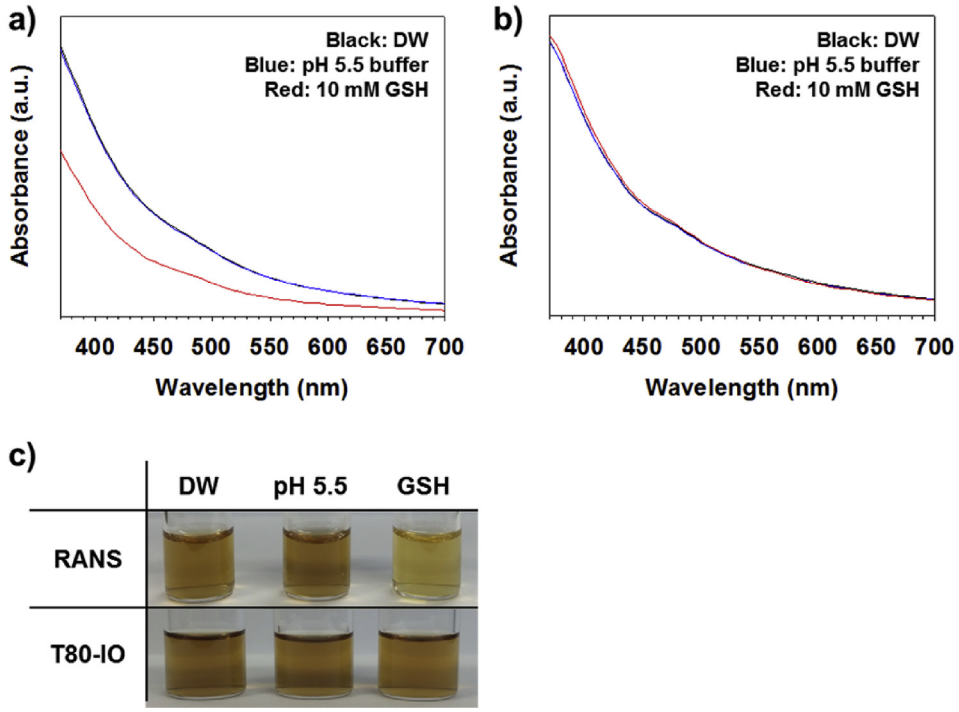

Fig. 4. UV–vis absorbance graphs of a) RANS and b) polysorbate 80-coated iron oxide (P80-IO) in DW (black), pH 5.5 buffer solution (blue), and 10 mM GSH solution (red), respectively. c) Photograph of the RANS and P80-IO in DW, pH 5.5 buffer solution, and 10 mM GSH solution. (For interpretation of the references to colour in this figure legend, the reader is referred to the web version of this article.)

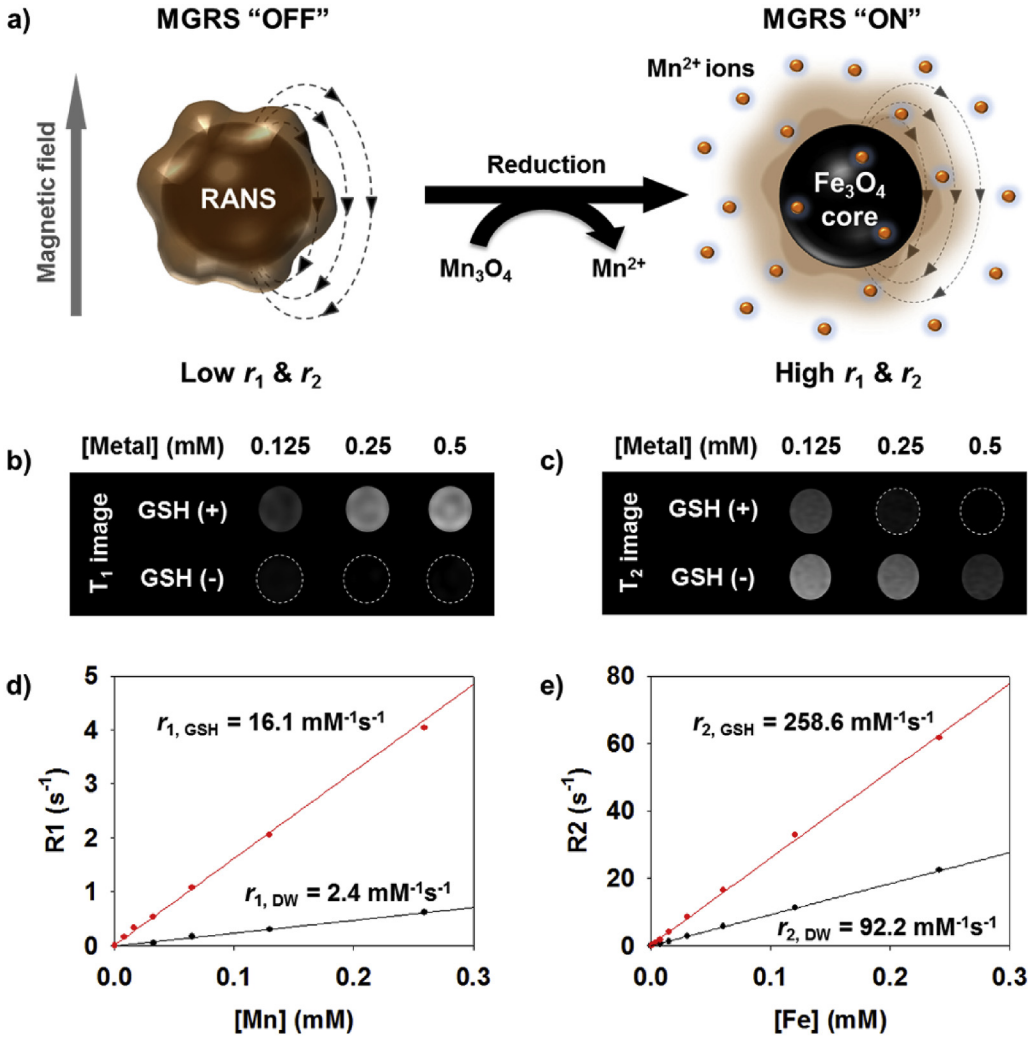

Fig. 5. MR imaging contrast effects of RANS. a) Possible mechanism of magnetic relaxation switch (MGRS) in RANS for activatable MR imaging. b) T_1 and c) T_2-weighted image of the RANS after treatment of GSH (10 mM) and non-treatment. d, e) Relaxivity plot of R1 and R2 vs concentration of the metal (Mn, Fe).

proton relaxation interference caused by the magnetic coupling effect between the T_1 materials (Mn_3O_4 shells or Mn centers) and T_2 materials (Fe_3O_4 cores) was attenuated. These results suggest that the MGRS of RANS is effectively activated under a reducing environment and demonstrates a dramatic enhancement in the T_1/T_2 MR contrast effect.

In order to assess their usefulness for biological applications, the cytotoxicity of RANS was first evaluated on human gastric cancer cell line MKN-45. After incubation with RANS for 24 h, the cell viability of MKN-45 cells remained high (over 80%) without any inhibitory effects on the growth or proliferation at concentrations below 14 μg_{metal} mL^{-1} (Fig. 6a). Mn^{2+} ions ($MnCl_2$) also showed similar cell viability at low metal concentrations; however, significant cell death (with survival less than 50%) was observed at 14 μg_{metal} mL^{-1}. This might be due to the gradual degradation of Mn_3O_4 and the remaining Mn^{2+} ions in the organic coating of RANS as opposed to the direct influx of metal ions, which could mitigate the cellular toxicity of free Mn^{2+} in the MKN-45 cells [35,36]. In Fig. 6b, the considerable number of black dots in the MKN-45 cell treated with RANS indicates the internalization of RANS into the cytoplasm without damaging the cellular structures. We investigated the T_1/T_2 MR contrast effect of RANS at the cellular level by performing MR imaging on MKN-45 cells at 1.5 T. The incubation of RANS with MKN-45 cells led to a pronounced enhancement in the T_1 and T_2 contrast as the concentration of the treated nanoprobes increased (1, 2, and 5 μg_{metal} mL^{-1}) (Fig. 6c). The MR signal intensity ratio, which represents the relaxation ratio ($R = T^{-1}$) difference between RANS-treated cells and non-treated cells ($\Delta R/R_{Non\text{-}treat}$, where $\Delta R = |R - R_{Non\text{-}treat}|$), showed remarkable MR imaging performance with significantly enhanced contrast in the MKN-45 cells treated with RANS; for a 5 μg_{metal} mL^{-1} treatment, this increase was up to 187.9% in the T_1-weighted image ($\Delta R1/R1_{Non\text{-}treat}$) and 338.5% in the T_2-weighted image ($\Delta R2/R2_{Non\text{-}treat}$) (Fig. 6e). To verify the influence of GSH on the activatable T_1/T_2 imaging ability of RANS in tumor cells, we used *N*-ethylmaleinide (NEM; a GSH scavenger) to modulate the intracellular GSH concentration [23,34]. The MKN-45 cells were incubated with NEM (0.01 mM or 0.05 mM) 10 min prior to incubation with RANS (5 μg_{metal} mL^{-1}). Cells were subsequently collected for MR imaging. As seen in Fig. 6d and f, the NEM-pretreated cells showed a noticeable loss of contrast in both the T_1- and T_2-weighted images. The R1 and R2 values also decreased compared to those of the free medium-pretreated cells. This is caused by the fact that NEM decreased the intracellular GSH concentration [23,34]; the dissolution of Mn_3O_4 shells was negligible, which decreased the subsequent activation of RANS. In parallel experiments, we observed strong T_1/T_2 MR contrast effects of RANS

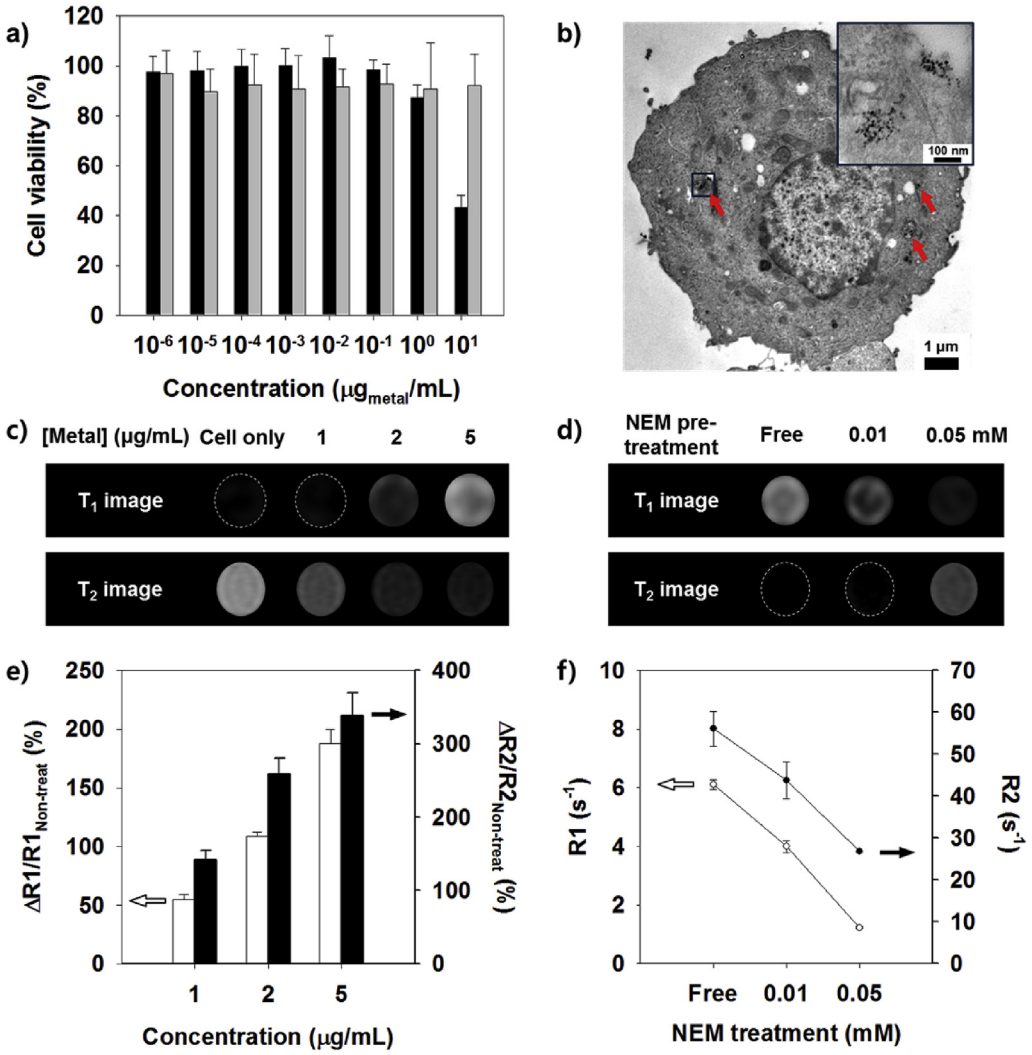

Fig. 6. a) Cell viability of the MKN-45 cells treated with various concentrations of Mn^{2+} (Black bars) and RANS (gray bars) (Highest concentration: 14 μg_{metal} mL^{-1}). b) Cross-sectional TEM image of MKN-45 cells incubated with RANS (inset: magnified image of intracellular internalized RANS). The internalized RANS is located in the cytoplasm. c) T_1- and T_2-weighted MR images of the MKN-45 cells after treatment of various concentrations of RANS (0, 1, 2, and 5 μg_{metal} mL^{-1}). d) T_1- and T_2-weighted MR images of the MKN-45 cells showing the change in the MR signal intensity upon varying intracellular GSH concentration of the cells by pre-treatment of NEM (a GSH scavenger) before the treatment of RANS (5 μg_{metal}/mL). e) The relative relaxation rate ($\Delta R/R_{non\text{-}treat}$, %, $\Delta R = R\text{-}R_{non\text{-}treat}$ and $R = T^{-1}$) of MKN-45 cells after RANS treatment versus non-treated cells obtained from c) (white bar: $\Delta R1/R1_{non\text{-}treat}$, black: bar: $\Delta R2/R2_{non\text{-}treat}$). f) The T_1 and T_2 relaxation rate (R1 and R2) measured from d).

for MKN-45 cells pretreated with α-lipoic acid (LA; a GSH synthesis enhancer: 0.05 mM and 0.1 mM), which were similar to those exhibited by free medium-pretreated cells (Fig. S6) [23,34,37]. Thus, we concluded that intracellular GSH was strongly related to the efficacy of the T_1/T_2 MR imaging capabilities of RANS. Additionally, the GSH level of the intracellular environment was sufficient to activate RANS in the tumor cells.

To demonstrate the feasibility of RANS as a T_1/T_2 DMCA for *in vivo* applications, we performed MR imaging of MKN-45 tumor-bearing nude mice injected *via* the tail vein with RANS (200 μL, 7 mg_{Fe+Mn} kg^{-1} mouse body weight). After administration in the bloodstream, the RANS favors extravasations through leaky tumor vasculature with hyper-permeability due to their relatively small size (21.9 nm) and surface properties (PEGylation for stealth coating) [16]. This was followed by deep penetration and retention at the tumor tissue (the EPR effect) [32,33]. In Fig. 7a, the T_1-weighted images showed obvious positive signal enhancement in the tumor sites after injection of RANS, as compared with the pre-injection image, while the tumor signals from T_2-weighted images became darker. Such a significant change in the MR contrast at the tumor was attributed to accumulation in the tumor (*via* the EPR effect) and the subsequent activation of RANS. To obtain quantitative and dependable results for signal intensity measurements, we analyzed the MR signal in the tumor by drawing ROIs of whole tumor volumes on both the T_1- and T_2-weighted images (Fig. 7b). The T_1 signal intensity increased sharply after administration of RANS and gradually grew by 49.8% at a post-injection time of 2 h; alternatively, the T_2 signal intensity was decreased to 63.7% of the value of the pre-injection scans. The H&E stained image and Prussian blue stained image showed the tumor sections and accumulation of RANS in the tumors (Fig. S7). These results indicated that RANS simultaneously provided both distinct positive T_1 and negative T_2 contrast enhancement in the MR imaging of tumors. The dual-contrast enhancing effect of this nanoprobe enables the synergistic combination of the two relaxation effects for accurate diagnosis of vague tumor sites. To investigate the *in vivo* toxicity after administration of RANS, the main organs (brain, heart, liver, kidney, lung, and spleen) of healthy mice (control) and RANS-

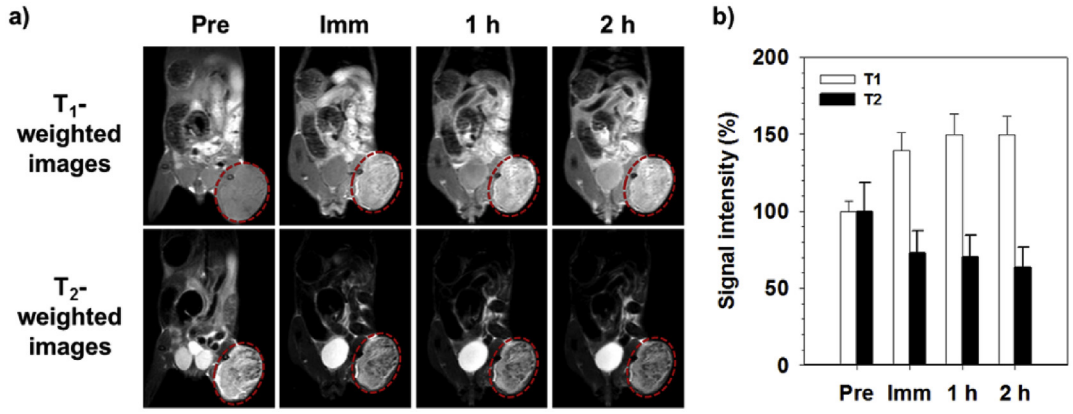

Fig. 7. a) In vivo T_1- and T_2-weighted MR images of MKN-45 tumor-bearing mice obtained before (Pre) and after (immediate, 1 h, and 2 h) the intravenous injection of RANS. b) Relative T_1 and T_2 signal intensities (%) of tumor sites (red dotted circle) at different time points. (For interpretation of the references to colour in this figure legend, the reader is referred to the web version of this article.)

treated mice (7 mg_{Fe+Mn} kg^{-1} mouse body weight) were collected 18 days after RANS treatment. Notably, the mice behaved normally without any noticeable sign of toxic side effect for the period after treatment of RANS. No appreciable sign of organ damage or inflammatory lesion was noticed for mice 18 days after RANS treatment compared to the healthy control mice, as revealed by H&E stained major organ slices of those mice (Fig. S8). Therefore, our RANS would be a safe candidate of MR imaging agent for *in vivo* use.

4. Conclusions

In summary, a smart activatable imaging nanoplatform (i.e., RANS) was designed and synthesized for T_1/T_2 dual-mode MR imaging by considering the structure-proton relaxation relationships in the nanosystem. We successfully developed hetero-nanocrystals by fusing superparamagnetic Fe_3O_4 cores and redox-responsive paramagnetic Mn_3O_4 shells. This forms a magnetic relaxation switch (MGRS) that is based on the change of water molecule interactions and the attenuation of the magnetic coupling effect after decomposition of the Mn_3O_4 in a reducing environment to dramatically enhance the MR contrast. Upon arrival and introduction to a tumor intracellular reducing environment, the Mn_3O_4 shells are decomposed to release free Mn^{2+} ions through a GSH/Mn_3O_4 redox reaction, which exposes the interior Fe_3O_4 cores to the aqueous environment. The fabricated RANS, which has a relatively small mean hydrodynamic size (21.9 nm), exhibited greatly increased r_1 (6.8-fold increase) and r_2 (2.8-fold increase) relaxivities. This improvement is due to the collective activation of the released free Mn^{2+} ions and the interior Fe_3O_4 cores, which occurs after the redox-mediated peeling of Mn_3O_4 shells in the reducing conditions (GSH solution). We also demonstrated the potential utility of RANS as an MR imaging agent. RANS shows synergistic dual-contrast enhancing capabilities in cellular/animal studies and exhibits clear brightening (positive) or darkening (negative) contrast in the T_1-or T_2-weighted MR images, respectively, for cancer detection. Through this approach, we believe that the features of RANS can be further extended and developed to new nanoplatforms with high imaging performance for a wide range of biological applications in the near future.

Acknowledgements

This work was supported by the Bio & Medical Technology Development Program of the National Research Foundation (NRF) funded by the Korean government (MEST) (Grant 2012050077). This work was also supported by the Bio & Medical Technology Development Program of the National Research Foundation (NRF) funded by the Ministry of Science, ICT & Future Planning (NRF-2015M3A9D7029878).

Appendix A. Supplementary data

Supplementary data related to this article can be found at http://dx.doi.org/10.1016/j.biomaterials.2016.05.054.

References

[1] A. Ahmed, C. Zhang, J. Guo, Y. Hu, X. Jiang, Fabrication and characterization of Gd-DTPA-Loaded chitosan-poly(acrylic acid) nanoparticles for magnetic resonance imaging, Macromol. Biosci. 15 (2015) 1105–1114.
[2] C.E. Smith, D. Ernenwein, A. Shkumatov, N.E. Clay, J. Lee, M. Melhem, et al., Hydrophilic packaging of iron oxide nanoclusters for highly sensitive imaging, Biomaterials 69 (2015) 184–190.
[3] G.D. Kenny, C. Villegas-Llerena, A.D. Tagalakis, F. Campbell, K. Welser, M. Botta, et al., Multifunctional receptor-targeted nanocomplexes for magnetic resonance imaging and transfection of tumours, Biomaterials 33 (2012) 7241–7250.
[4] D. Yoo, J.H. Lee, T.H. Shin, J. Cheon, Theranostic magnetic nanoparticles, Acc. Chem. Res. 44 (2011) 863–874.
[5] N.A. Keasberry, M. Banobre-Lopez, C. Wood, G.J. Stasiuk, J. Gallo, N.J. Long, Tuning the relaxation rates of dual-mode T(1)/T(2) nanoparticle contrast agents: a study into the ideal system, Nanoscale 7 (2015) 16119–16128.
[6] T. Kim, E.J. Cho, Y. Chae, M. Kim, A. Oh, J. Jin, et al., Urchin-shaped manganese oxide nanoparticles as pH-responsive activatable T1 contrast agents for magnetic resonance imaging, Angew. Chem. Int. Ed. Engl. 50 (2011) 10589–10593.
[7] K.N. Raymond, V.C. Pierre, Next generation, high relaxivity gadolinium MRI agents, Bioconjug. Chem. 16 (2005) 3–8.
[8] T. Tegafaw, W. Xu, M.W. Ahmad, J.S. Baeck, Y. Chang, J.E. Bae, et al., Dual-mode T1 and T2 magnetic resonance imaging contrast agent based on ultrasmall mixed gadolinium-dysprosium oxide nanoparticles: synthesis, characterization, and in vivo application, Nanotechnology 26 (2015) 365102.
[9] M.H. Kim, B. Kim, E.K. Lim, Y. Choi, J. Choi, E. Kim, et al., Magnetic nanoclusters engineered by polymer-controlled self-assembly for the accurate diagnosis of atherosclerotic plaques via magnetic resonance imaging, Macromol. Biosci. 14 (2014) 943–952.
[10] R. Hao, J. Yu, Z. Ge, L. Zhao, F. Sheng, L. Xu, et al., Developing Fe3O4 nanoparticles into an efficient multimodality imaging and therapeutic probe, Nanoscale 5 (2013) 11954–11963.
[11] X. Wang, D. Niu, Q. Wu, S. Bao, T. Su, X. Liu, et al., Iron oxide/manganese oxide co-loaded hybrid nanogels as pH-responsive magnetic resonance contrast agents, Biomaterials 53 (2015) 349–357.
[12] N. Lee, Y. Choi, Y. Lee, M. Park, W.K. Moon, S.H. Choi, et al., Water-dispersible ferrimagnetic iron oxide nanocubes with extremely high r(2) relaxivity for highly sensitive in vivo MRI of tumors, Nano Lett. 12 (2012) 3127–3131.
[13] T.H. Shin, J.S. Choi, S. Yun, I.S. Kim, H.T. Song, Y. Kim, et al., T(1) and T(2) dual-mode MRI contrast agent for enhancing accuracy by engineered nanomaterials, ACS Nano 8 (2014) 3393–3401.
[14] Z. Zhou, D. Huang, J. Bao, Q. Chen, G. Liu, Z. Chen, et al., A synergistically enhanced T(1) -T(2) dual-modal contrast agent, Adv. Mater. 24 (2012)

6223–6228.
[15] J.S. Choi, J.H. Lee, T.H. Shin, H.T. Song, E.Y. Kim, J. Cheon, Self-confirming "AND" logic nanoparticles for fault-free MRI, J. Am. Chem. Soc. 132 (2010) 11015–11017.
[16] K. Cheng, M. Yang, R. Zhang, C. Qin, X. Su, Z. Cheng, Hybrid nanotrimers for dual T1 and T2-weighted magnetic resonance imaging, ACS Nano 8 (2014) 9884–9896.
[17] G.H. Im, S.M. Kim, D.G. Lee, W.J. Lee, J.H. Lee, I.S. Lee, Fe(3)O(4)/MnO hybrid nanocrystals as a dual contrast agent for both T(1)- and T(2)-weighted liver MRI, Biomaterials 34 (2013) 2069–2076.
[18] K.S. Kim, W. Park, J. Hu, Y.H. Bae, K. Na, A cancer-recognizable MRI contrast agents using pH-responsive polymeric micelle, Biomaterials 35 (2014) 337–343.
[19] Y. Chen, K. Ai, J. Liu, X. Ren, C. Jiang, L. Lu, Polydopamine-based coordination nanocomplex for T1/T2 dual mode magnetic resonance imaging-guided chemo-photothermal synergistic therapy, Biomaterials 77 (2016) 198–206.
[20] Z. Zhao, H. Fan, G. Zhou, H. Bai, H. Liang, R. Wang, et al., Activatable fluorescence/MRI bimodal platform for tumor cell imaging via MnO2 nanosheet-aptamer nanoprobe, J. Am. Chem. Soc. 136 (2014) 11220–11223.
[21] M.L. Viger, J. Sankaranarayanan, C. de Gracia Lux, M. Chan, A. Almutairi, Collective activation of MRI agents via encapsulation and disease-triggered release, J. Am. Chem. Soc. 135 (2013) 7847–7850.
[22] G.K. Such, Y. Yan, A.P. Johnston, S.T. Gunawan, F. Caruso, Interfacing materials science and biology for drug carrier design, Adv. Mater. 27 (2015) 2278–2297.
[23] J. Lai, B.P. Shah, E. Garfunkel, K.B. Lee, Versatile fluorescence resonance energy transfer-based mesoporous silica nanoparticles for real-time monitoring of drug release, ACS Nano 7 (2013) 2741–2750.
[24] D. He, X. He, K. Wang, X. Yang, X. Yang, Z. Zou, et al., Redox-responsive degradable honeycomb manganese oxide nanostructures as effective nanocarriers for intracellular glutathione-triggered drug release, Chem. Commun. Camb. 51 (2015) 776–779.
[25] W. Cheng, G. Wang, X. Pan, Y. Zhang, B.Z. Tang, Y. Liu, Redox-responsive nanoparticles with Aggregation-Induced Emission (AIE) characteristic for fluorescence imaging, Macromol. Biosci. 14 (2014) 1059–1066.
[26] J. Carretero, E. Obrador, M.J. Anasagasti, J.J. Martin, F. Vidal-Vanaclocha, J.M. Estrela, Growth-associated changes in glutathione content correlate with liver metastatic activity of B16 melanoma cells, Clin. Exp. Metastasis 17 (1999) 567–574.
[27] G.S. Loving, S. Mukherjee, P. Caravan, Redox-activated manganese-based MR contrast agent, J. Am. Chem. Soc. 135 (2013) 4620–4623.
[28] F.J. Douglas, D.A. MacLaren, F. Tuna, W.M. Holmes, C.C. Berry, M. Murrie, Formation of octapod MnO nanoparticles with enhanced magnetic properties through kinetically-controlled thermal decomposition of polynuclear manganese complexes, Nanoscale 6 (2014) 172–176.
[29] V.N. Phan, E.K. Lim, T. Kim, M. Kim, Y. Choi, B. Kim, et al., A highly crystalline manganese-doped iron oxide nanocontainer with predesigned void volume and shape for theranostic applications, Adv. Mater. 25 (2013) 3202–3208.
[30] S. Zhang, X. Qian, L. Zhang, W. Peng, Y. Chen, Composition-property relationships in multifunctional hollow mesoporous carbon nanosystems for PH-responsive magnetic resonance imaging and on-demand drug release, Nanoscale 7 (2015) 7632–7643.
[31] K.L. Krycka, J.A. Borchers, G. Salazar-Alvarez, A. Lopez-Ortega, M. Estrader, S. Estrade, et al., Resolving material-specific structures within Fe(3)O(4)|gamma-Mn(2)O(3) core|shell nanoparticles using anomalous small-angle X-ray scattering, ACS Nano 7 (2013) 921–931.
[32] R.A. Petros, J.M. DeSimone, Strategies in the design of nanoparticles for therapeutic applications, Nat. Rev. Drug Discov. 9 (2010) 615–627.
[33] T. Stylianopoulos, EPR-effect: utilizing size-dependent nanoparticle delivery to solid tumors, Ther. Deliv. 4 (2013) 421–423.
[34] R. Deng, X. Xie, M. Vendrell, Y.T. Chang, X. Liu, Intracellular glutathione detection using MnO(2)-nanosheet-modified upconversion nanoparticles, J. Am. Chem. Soc. 133 (2011) 20168–20171.
[35] A. Wang, M. Guo, N. Wang, J. Zhao, W. Qi, F. Muhammad, et al., Redox-mediated dissolution of paramagnetic nanolids to achieve a smart theranostic system, Nanoscale 6 (2014) 5270–5278.
[36] S.H. Bhang, J. Han, H.K. Jang, M.K. Noh, W.G. La, M. Yi, et al., pH-triggered release of manganese from MnAu nanoparticles that enables cellular neuronal differentiation without cellular toxicity, Biomaterials 55 (2015) 33–43.
[37] B. Hultberg, A. Andersson, A. Isaksson, Lipoic acid increases glutathione production and enhances the effect of mercury in human cell lines, Toxicology 175 (2002) 103–110.